

Vibrational Spectroscopic Detection of Single Virus by a Confocal Interferometric Mid-Infrared Photothermal Microscope

Yi Zhang^[a], Alexander J. Devaux^[b], John H. Connor*^[c], and Ji-Xin Cheng*^[a,d]

[a] Y. Zhang
Department of Physics
Boston University
590 Commonwealth Avenue # 255, Boston, MA 02215
E-mail: zhangyi@bu.edu

[b] Senior Research Technician. A.J. Devaux
School of Medicine - Microbiology
Boston University
72 E Concord St, Boston, MA 02118
E-mail: ajdevaux@bu.edu

[c] Professor, J. H. Connor
School of Medicine - Microbiology
Boston University
72 E Concord St, Boston, MA 02118
E-mail: jhconnor@bu.edu

[d] Professor, J. X. Cheng
Department of Electrical and Computer Engineering, Department of Biomedical Engineering
Boston University
8 St Marys St # 324, Boston, MA 02215
E-mail: jxcheng@bu.edu

Abstract: We report a confocal interferometric mid-infrared photothermal (MIP) microscope and its application to label-free detection of biological nanoparticles down to single virus level. We apply the interferometric scattering principle to detect the weak photothermal effect induced by infrared absorption in a viral particle. We validated this method with two kinds of viruses, namely vesicular stomatitis virus (VSV) and poxvirus. The single virus spectra generated by MIP microscopy show high consistency in the same group, with dominant peaks contributed by the amide I and amide II vibrations. The ratio of these two peaks are significantly different between VSV and poxvirus, highlighting the potential of using MIP microscopy for label-free differentiation of viral particles. This all-optical chemical imaging method opens a new way for spectroscopic detection of biological nanoparticles in a label-free manner and may facilitate in predicting and controlling outbreaks of emerging virus strains.

Viruses exist wherever life is found. Genetically diverse and evolving rapidly^[1], viruses are responsible for a numerous epidemic outbreaks, including the zoonotic H5N1 pandemic^[2], Zika^[3], Ebola^[4], and the ongoing COVID-19^[5]. Rapid identifying unknown viruses would aid in preparation for future outbreaks^[6].

Existing diagnosis methods, including the immune-based, enzyme-linked immunosorbent assay (ELISA)^[7] and the polymerase chain reaction (PCR) technique^[8], provide relatively sensitive detection and identification of virus. The nucleic acid tests for infectious disease are primarily based on amplification methods that use primers and probes designed to detect specific organisms. Because a prior knowledge of nucleic acid sequence information is required, the nucleic acid tests are not able to identify unanticipated, newly emergent, or previously unknown infectious organisms. Thus, discovery of new infectious organisms relies largely on culture methods^[9] and microscopy tools^[10].

Optical microscopy has been a fundamental tool in life science since the discovery of bacteria as “small animals” by Van Leeuwenhoek using his bright field microscope three centuries ago. Related to virus detection, a novel optical imaging technique based on interferometric scattering (iSCAT) pushes the sensitivity

beyond the bright-field optical microscope^[11]. The principle of iSCAT microscopy is that light scattered from a nanoparticle of interest is interfered with a brighter reference field to make single nanoparticles detectable^[12]. Yet, this method is based on Raleigh scattering and does not provide molecular information.

To obtain molecular information, Raman scattering and infrared absorption spectroscopy are commonly used to identify the chemical content of a substance based on molecular vibrational fingerprints. For Raman scattering, the cross section is extremely small – approximately 1 out of 10^{10} incident photons is emitted through Raman scattering. Surface-enhanced Raman scattering (SERS) has shown great potential for single molecule detection at a plasmatic hot spot^[13]. The detection reliability of SERS is however relied on the quality of the substrate. In addition, because the hot spot (< 10 nm) is smaller than a virus (~ 100 nm), SERS is not able to probe the entire content of a virus. Tip-enhanced Raman spectroscopy (TERS) detection of virus is reported^[14], where the reliability strongly depends on the tip quality.

Compare with Raman scattering, infrared absorption has a much larger cross section^[15]. The infrared spectra deliver information on proteins as well as on interactions between protein subunits and nucleic acids^[16]. Yet, spectroscopic detection of a single virus by conventional FTIR is hampered by the intrinsically low spatial resolution on the micron scale^[17]. AFM-IR, which offers nanoscale spatial resolution and high detection sensitivity, is capable of providing single virus infrared spectrum^[18]. Yet, AFM-IR requires sample contact, thus suffering sample damage risk. Thus, a contact-free, easy to operate, and highly sensitive method for single virus detection is desired.

Mid-infrared photothermal (MIP) imaging is an emerging technique^[19] meeting these requirements. In MIP microscopy, a visible beam is deployed to sense the photothermal effect induced by infrared absorption of molecules, providing sub-micron spatial resolution defined by the visible probe beam. MIP signals can be detected in either scanning mode^[19] or wide-field mode^[20]. On the excitation side, MIP can be implemented with an IR/Visible co-propagating or counter-propagating geometry. In the latter, a high numerical aperture objective lens can be used to focus the visible beam and a spatial resolution of 300 nm has been reached^[19d]. Here, we harness the iSCAT principle and confocal detection to push the biological detection limit of MIP microscopy to an unprecedented level towards single virus detection. We report, for

the first time, vibrational fingerprint spectra of poxvirus and vesicular stomatitis virus (VSV) recorded with a counter-propagating confocal MIP microscope.

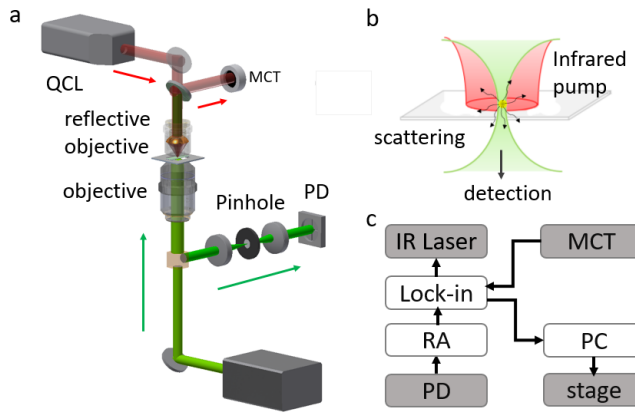


Figure 1. Principle and schematic of MIP imaging. (a) Setup. A pulsed mid-infrared pump beam is provided by a QCL laser and focused by a reflective objective. A continuous probe laser beam is focused at the sample by a water immersion objective. Part of the infrared laser is reflected by CaF₂ and is measured by a mercury cadmium telluride (MCT) detector. The back-scattered probe beam is collected through a pinhole and detected by a silicon photodiode (PD). (b) illustration of counter-propagating IR and visible beams at the focus. (c) Electronics connection. The probe beam is detected by a PD and the photothermal signal is demodulated by a lock-in amplifier (LIA). A PC is used to control the scanning stage and data acquisition. The IR intensity detected by MCT is also received by LIA for normalization of the photothermal signal by IR power at each wavelength. The lock-in sends a reference signal to trigger the laser at 100 kHz frequency.

A schematic of our setup is shown in **Figure 1**. A pulsed mid-IR pump beam, generated by a tunable (from 1000 to 1886 cm⁻¹) quantum cascade laser (QCL, Daylight Solutions, MIRcat-2400) operating at 100 kHz repetition rate, passes through a calcium fluoride (CaF₂) cover glass and then is focused onto the sample through a gold-coating reflective objective lens (52x; NA, 0.65; Edmund Optics, #66589). A continuous-wave probe laser (Cobolt, Samba 532 nm) beam is focused onto the same spot from the opposite side by a high NA refractive objective (60x; NA, 1.2; water immersion; Olympus, UPlanSApo). The probe beam is aligned to be collinear to the mid-IR pump beam to ensure the overlap of the two foci to achieve a good signal level. A scanning piezo stage (Mad City Labs, Nano-Bio 2200) with a maximum scanning speed of 200 μ s/pixel is used to scan the sample. Before the photodiode, a confocal pinhole is placed to pass the scattered photons from the nanoparticles and the reflected photons from the top surface of CaF₂ glass, but block the photons reflected from other surfaces. In the imaging procedure, the nanoparticles spotted on a CaF₂ cover glass are first localized by the backward iSCAT signal. The sample stage is adjusted axially to maximize the iSCAT contrast. Then, the pulsed infrared pump is on. The modulated scattering is collected by a photodiode and the MIP signal is extracted by a lock-in amplifier. Before the reflective objective, the infrared laser passes through a CaF₂ slip and the reflection of the infrared laser is measured by a mercury cadmium telluride (MCT) detector for normalization of IR power at each wavelength. A laboratory-built resonant circuit, with its resonant frequency (103.8 kHz, gain 100) tuned to repetition rate of the QCL laser, is used to amplify the photocurrent from the photodiode before it is sent to the lock-in amplifier (Zurich Instruments, HF2LI) for phase-sensitive detection of the MIP signal.

To process the signal, the power of the mid-IR beam collected by the MCT detector is sent to another lock-in input channel. A computer is used to synchronize the QCL wavelength selection, stage scanning, and data acquisition. The photothermal spectra were processed under an MATLAB environment using in-house scripts. The raw photothermal signal was normalized by the mid-infrared laser power spectrum collected by the MCT detector at a step size of 5 cm⁻¹. For detection of virus, the photothermal spectra were averaged 5 times to achieve high signal to noise ratio (SNR).

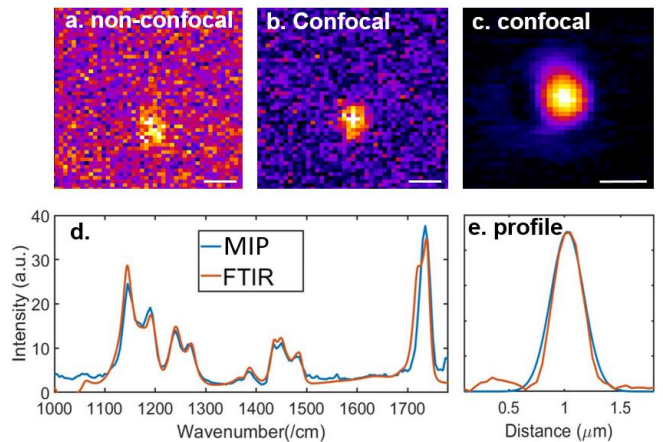


Figure 2. Performance of MIP microscope. (a) MIP of 200 nm PMMA beads without confocal pinhole, 2 ms pixel dwell time (b) MIP of 200 nm PMMA beads with confocal pinhole, 2 ms pixel dwell time. (c) MIP image of 200 nm PMMA beads with confocal detection, 20 ms pixel dwell time. Scale bar: 500 nm. Image acquisition time: 32 s; Probe power on the sample: 30 mW; IR pump power on the sample: 5 mW at 1729 cm⁻¹. Intensity: arbitrary unit. (d) MIP spectrum obtained from a single PMMA bead and FTIR acquired from a PMMA film. MIP acquisition time: 10 ms per wavenumber. (e) The horizontal intensity profiles across the bead at the 1730 cm⁻¹ peak (Figure 2c). The measured full width at half maximum (FWHM) was 380 nm. After deconvolution by particle diameter, we obtain a spatial resolution of 260 nm. This value is in consistence with previous studies using the same counter-beam geometry^[19e].

We first evaluated the sensitivity of the MIP system by measuring 200-nm diameter poly (methyl methacrylate) (PMMA) beads. The particle size resembles the viral particles to be measured. **Figure 2a** shows a non-confocal MIP image of a single PMMA bead. By modifying the system to be confocal, the noise is suppressed and an image with improved SNR is shown in **Figure 2b**. To obtain even higher quality, we extended the dwell time of each pixel from 2 ms to 20 ms and applied smaller pixel step size. A much improved image with a SNR of 96 is shown in **Figure 2c**. All images were taken by tuning the IR laser to 1730 cm⁻¹, in resonance with acrylate carboxyl group absorption in PMMA. The spectral fidelity is confirmed by comparing the MIP spectral profile to the reference spectrum of PMMA collected by a FTIR spectrometer (**Figure 2d**). To evaluate the spatial resolution of MIP, we measured the intensity profile across the bead at the 1730 cm⁻¹ peak (**Figure 2e**). The measured full width at half maximum (FWHM) was 380 nm. After deconvolution by particle diameter, we obtain a spatial resolution of 260 nm. This value is in consistence with previous studies using the same counter-beam geometry^[19e].

On the basis of the above characterization, we explored the potential of MIP microscopy for single virus detection. we tested two kinds of virus: rVSV-G-eGFP (VSV) and rVACV-A4L-Venus (poxvirus) which were generated as described^[21]. To load the virus onto a viewing surface, 100 μ L of either VSV or poxvirus stock was incubated on a CaF₂ coverslip for 1 hour at room temperature. The VSV concentration was ~3x10⁸ PFU/mL and the poxvirus concentration was ~2x10⁸ PFU/mL. Following incubation, coverslips were examined with fluorescence microscopy to ensure that virus was present. All virions were

crosslinked and inactivated using 1.0 mL 4% formaldehyde for 1 hour and then dried.

We choose poxvirus as our first testing model. Poxvirus belongs to a family of double stranded DNA viruses^[22]. They are brick-shaped (240 nm by 300 nm) with a well-packed internal structure. Under the spatial resolution of our microscope system, we did not expect to resolve the shape, but were able to measure it as a single particle. **Figure 3a** shows the iSCAT image of a poxvirus, where the scattering from the poxvirus is accompanied by a large background contributed by reflected photons. Importantly, the background photons interfere with the scattered photons and make the virus detectable. **Figure 3b** and **Figure 3c** display the MIP image of the same virus as shown in **Figure 3a**, with the IR laser tuned to 1650 cm^{-1} for the amide I band and 1550 cm^{-1} for the amide II band of proteins. Both images show high contrast because the background is removed through lock-in detection. In the iSCAT image of the poxvirus, the scattered photons after interference with the background photons generated 0.06 V signal on the photodiode and the background gave around 0.8 V signal. Thus, in the iSCAT image, we had around 7.5% image contrast, which allowed us to identify the virus particle. For the MIP signal, according to the input range, output signal level and internal amplification factor from the lock-in amplifier, the modulation depth is calculated to be around 0.1%. Such changes can be readily extracted by a lock-in amplifier, which allows background-free chemical imaging of the virus.

We then took MIP spectra in the fingerprint window (1000 to 1750 cm^{-1}). This procedure was repeated on four randomly chosen poxvirus. The spectra displayed high consistency, as shown in **Figure 3d**. We observed two dominated bands contributed by amide I and amide II vibrations, but negligible signal from the phosphate vibration at 1080 cm^{-1} . The virus has the well-organized structure that a protein shell covers the DNA inside of it. It is possible that vibrational absorption of DNA may not cause a particle size change measurable by MIP.

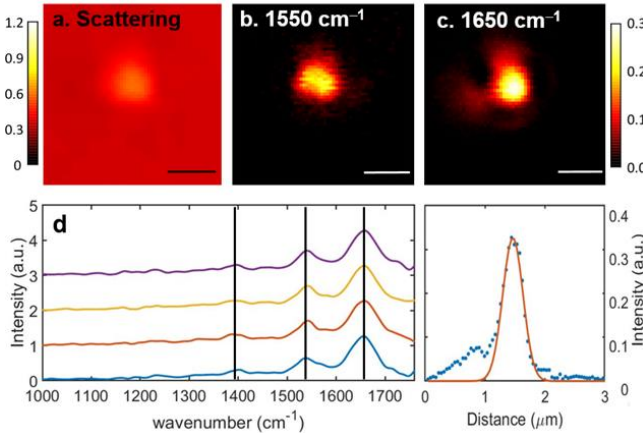


Figure 3. MIP imaging and spectroscopy of single poxviruses. (a) Scattering image of a poxvirus. Scale bar: 500 nm. Probe power 30 mW, dwell time 20 ms (b) MIP image of the same poxvirus at the 1550 cm^{-1} . Power 18 mW Scale bar 500 nm, pixel dwell time 20 ms. (c) MIP image of the same virus at the 1650 cm^{-1} power 20 mW. Scale bar: 500 nm, pixel dwell time 20 ms. The intensity profile across the virus is shown as a dotted curve below panel c. The intensity profile is fitted with a Gaussian profile. (d) MIP spectra of four randomly chosen poxviruses.

Next, to test whether our technology can differentiate different types of viruses, we performed MIP detection of VSV. **Figure 4a-b** shows the MIP image of two randomly chosen VSV. A high SNR was obtained in both images. Then, we acquired MIP spectra from the same two individual viruses. As shown in **Figure 4c**, the spectral profiles are highly repeatable. Importantly, we observed

significant differences between poxvirus and VSV. The amide I and amide II peaks are the major feature of the virus MIP spectrum. The amide I to amide II intensity ratio for poxvirus is found to be 0.51 and the ratio for the VSV is 0.42. Also, the gap between the amide I and amide II peaks is less obvious for VSV. These spectroscopic features are likely a reflection of the unit structure and molecular content of each virus and can be used to differentiate different kinds of viruses.

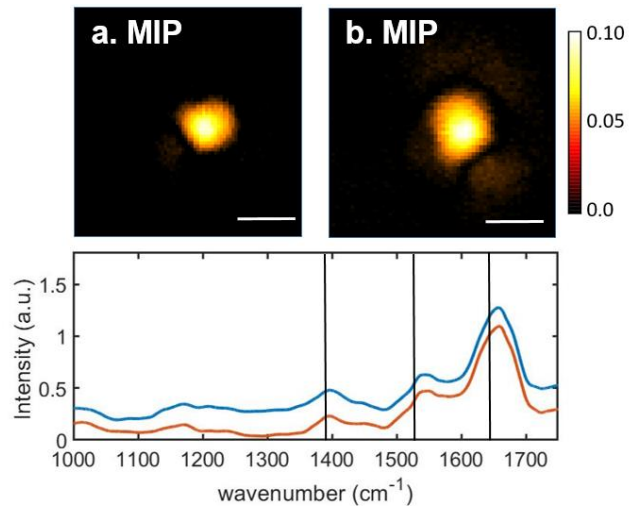


Figure 4. MIP imaging and spectroscopy of single VSV. (a, b) MIP image of individual VSV particles with the IR laser tuned to 1650 cm^{-1} . Power 20 mW. Probe power 30 mW. Scale bar: 500 nm, pixel dwell time 20 ms. (c) MIP spectra of the two VSV particles shown in panel a and b.

In summary, we have reported a counter-propagating confocal mid-infrared photothermal imaging system and its application to detection of single viruses. We harnessed the principle of interferometric scattering in order to probe the weak signal from a viral particle. Using this approach, we have recorded the fingerprint IR spectra from poxvirus and vesicular stomatitis virus. The dominant peaks are contributed by the amide I and amide II groups and the peak ratio allows differentiation of the two groups of viruses. Unlike SERS, our approach does not need plasmonic enhancement on a nanoparticle substrate. Collectively, mid-infrared photothermal microscopy as a pump-probe technique opens opportunities for label-free spectroscopic detection of single viruses and biological nanoparticles in general.

Acknowledgements

This work is supported by R01 GM126409 and R42 CA224844 to JXC.

Keywords: Viruses • IR spectroscopy • photothermal • chemical imaging

[1] aK. Y. B. r. givind Bergh, G. B. M. Heldal, *NATURE* **1989**, 340, 467-468; bK. Rosario, M. Breitbart, *Curr Opin Virol* **2011**, 1, 289-297; cE. V. Koonin, V. V. Dolja, *Current opinion in virology* **2013**, 3, 546-557.

[2] Y. Guan, L. Poon, C. Cheung, T. Ellis, W. Lim, A. Lipatov, K. Chan, K. Sturm-Ramirez, C. Cheung, Y. Leung, *Proceedings of the National Academy of Sciences* **2004**, 101, 8156-8161.

[3] A. R. Plourde, E. M. Bloch, *Emerging infectious diseases* **2016**, 22, 1185.

[4] S. Baize, D. Pannetier, L. Oestereich, T. Rieger, L. Koivogui, N. F. Magassouba, B. Soropogui, M. S. Sow, S. Keita, H. De Clerck, *New England Journal of Medicine* **2014**, 371, 1418-1425.

[5] F. Wu, S. Zhao, B. Yu, Y. M. Chen, W. Wang, Z. G. Song, Y. Hu, Z. W. Tao, J. H. Tian, Y. Y. Pei, M. L. Yuan, Y. L. Zhang, F. H. Dai, Y. Liu, Q. M. Wang, J. J. Zheng, L. Xu, E. C. Holmes, Y. Z. Zhang, *Nature* **2020**, 579, 265-269.

[6] W. I. Lipkin, S. J. Anthony, *Virology* **2015**, 479-480, 194-199.

[7] E. Engvall, P. Perlmann, *Protides of the biological fluids* **1971**, 553-556.

[8] F. Watzinger, K. Ebner, T. Lion, *Molecular aspects of medicine* **2006**, 27, 254-298.

[9] D. S. Leland, C. C. Ginocchio, *Clinical microbiology reviews* **2007**, 20, 49-78.

[10] C. S. Goldsmith, S. E. Miller, *Clinical microbiology reviews* **2009**, 22, 552-563.

[11] K. Lindfors, T. Kalkbrenner, P. Stoller, V. Sandoghdar, *Physical review letters* **2004**, 93, 037401.

[12] aO. Avci, N. L. Ünlü, A. Y. Özkumur, M. S. Ünlü, *Sensors* **2015**, 15, 17649-17665; bJ. Ortega-Arroyo, P. Kukura, *Physical Chemistry Chemical Physics* **2012**, 14, 15625-15636; cR. W. Taylor, V. Sandoghdar, *Nano letters* **2019**, 19, 4827-4835.

[13] aS. Nie, S. R. Emory, *science* **1997**, 275, 1102-1106; bX. Zhang, X. Zhang, C. Luo, Z. Liu, Y. Chen, S. Dong, C. Jiang, S. Yang, F. Wang, X. Xiao, *Small* **2019**, 15, 1805516; cV. I. Kukushkin, N. M. Ivanov, A. A. Novoseltseva, A. S. Gambaryan, I. V. Yaminsky, A. M. Kopylov, E. G. Zavyalova, *PLoS one* **2019**, 14; dY.-T. Yeh, K. Gulino, Y. Zhang, A. Sabestien, T.-W. Chou, B. Zhou, Z. Lin, I. Albert, H. Lu, V. Swaminathan, *Proceedings of the National Academy of Sciences* **2020**, 117, 895-901.

[14] K. Olschewski, E. Kämmer, S. Stöckel, T. Bocklitz, T. Deckert-Gaudig, R. Zell, D. Cialla-May, K. Weber, V. Deckert, J. Popp, *Nanoscale* **2015**, 7, 4545-4552.

[15] C. Matthäus, B. Bird, M. Miljković, T. Chernenko, M. Romeo, M. Diem, *Methods in cell biology* **2008**, 89, 275-308.

[16] aA. Barth, *Biochimica et Biophysica Acta (BBA)-Bioenergetics* **2007**, 1767, 1073-1101; bH. Tajmir-Riahi, C. N'Soukpo-Kossi, D. Joly, *Journal of Spectroscopy* **2009**, 23, 81-101.

[17] L. Hansen, T. De Beer, K. Pierre, S. Pastoret, A. Bonnegrade - Bernard, R. Daoussi, C. Vervae, J. P. Remon, *Biotechnology progress* **2015**, 31, 1107-1118.

[18] M. Brehm, T. Taubner, R. Hillenbrand, F. Keilmann, *Nano Letters* **2006**, 6, 1307-1310.

[19] aD. Zhang, C. Li, C. Zhang, M. N. Slipchenko, G. Eakins, J.-X. Cheng, *Science advances* **2016**, 2, e1600521; bC. Li, D. Zhang, M. N. Slipchenko, J.-X. Cheng, *Analytical chemistry* **2017**, 89, 4863-4867; cZ. Li, K. Aleshire, M. Kuno, G. V. Hartland, *The Journal of Physical Chemistry B* **2017**, 121, 8838-8846; dX. Li, D. Zhang, Y. Bai, W. Wang, J. Liang, J.-X. Cheng, *Analytical chemistry* **2019**, 91, 10750-10756; eI. M. Pavlovec, E. A. Podshivaylov, R. Chatterjee, G. V. Hartland, P. A. Frantsuzov, M. Kuno, *Journal of Applied Physics* **2020**, 127, 165101.

[20] aY. Bai, D. Zhang, L. Lan, Y. Huang, K. Maize, A. Shakouri, J.-X. Cheng, *Science advances* **2019**, 5, eaav7127; bD. Zhang, L. Lan, Y. Bai, H. Majeed, M. E. Kandel, G. Popescu, J.-X. Cheng, *Light: Science & Applications* **2019**, 8, 1-12; cM. Tamamitsu, K. Toda, H. Shimada, T. Honda, M. Takarada, K. Okabe, Y. Nagashima, R. Horisaki, T. Ideguchi, *Optica* **2020**, 7, 359-366; dM. Schnell, S. Mittal, K. Falahkheirkhah, A. Mittal, K. Yeh, S. Kenkel, A. Kajdacsy-Balla, P. S. Carney, R. Bhargava, *Proceedings of the National Academy of Sciences* **2020**, 117, 3388-3396.

[21] aA. N. van den Pol, K. P. Dalton, J. K. Rose, *Journal of virology* **2002**, 76, 1309-1327; bK. Dower, K. H. Rubins, L. E. Hensley, J. H. Connor, *Antiviral research* **2011**, 91, 72-80.

[22] S. C. Harrison, B. Alberts, E. Ehrenfeld, L. Enquist, H. Fineberg, S. L. McKnight, B. Moss, M. O'Donnell, H. Ploegh, S. L. Schmid, *Proceedings of the National Academy of Sciences* **2004**, 101, 11178-11192.

